SURFACE TREATMENT OF SUPERALLOYS BY LASER SKIN MELTING

E. M. Breinan,[+] B. H. Kear,[*] C. M. Banas[+] and L. E. Greenwald[+]

[+]United Technologies Research Center, East Hartford, Connecticut
[*]Pratt & Whitney Aircraft, Middletown, Connecticut

ABSTRACT

A new process for the surface treatment of metals and alloys using lasers
is described. Processing is accomplished by rapidly traversing a continuous,
highly focused laser beam over the material surface. The high specific rate
of energy delivery results in surface localized melting of a thin layer with
high melting efficiency, i.e., a major fraction of the absorbed energy causes
melting and a substantially smaller fraction goes into heating the substrate.
This ability to melt a thin surface layer while maintaining a cold substrate
results in rapid quenching of the molten layer by the bulk solid due to the
intimate contact at the interface. It is calculated that cooling rates up to
5×10^8 °C/sec are possible in 2.5×10^{-3} mm thick melt layers in nickel-base
alloys. For 2.5×10^{-2} mm thick layers, the cooling rates are up to 5×10^6
°C/sec.

A variety of metallurgical structures have been produced in nickel-base
alloys by this process. Typically, multicomponent nickel-base superalloys
yield an extremely fine dendritic structure of supersaturated γ matrix phase,
with interdendritic regions composed of fine particles of MC carbide and/or
γ/γ' eutectic, depending on alloy composition. Eutectic superalloys also de-
velop dendritic structures, but the interdendritic regions are more complex in
structure. For example, eutectic alloys containing a high volume fraction of
MC carbide exhibit an extremely fine filamentary structure. In all cases,
oriented overgrowth, or epitaxial growth is the characteristic feature of the
skin melted material. Epitaxial growth is particularly favored on a cube ori-
ented monocrystalline substrate.

Potential applications involving erosion, corrosion, wear and fatigue resis-
tant surface coatings for superalloys are briefly discussed. The process has
been utilized as a reproducible screening technique for alloy design.

Introduction

Many techniques have been devised for the rapid cooling of metals and alloys from the melt. Duwez and co-workers[1-3] introduced the 'gun' technique in which a pressurized inert gas is used to propel small globules of melt against a cold copper substrate. The technique has been widely used to obtain small samples of somewhat irregularly-shaped thin foils or powders with cooling rates typically in the range 10^6-10^8°C/sec. Pietrokowsky[4] developed the 'piston and anvil' technique, in which a droplet of melt is flattened between rapidly moving compression platens of copper. This technique yields samples in the form of thin plates of uniform thickness with cooling rates in the range 10^6-10^7°C/sec. Subsequent developments have included combining the two techniques, as in the 'gun and piston-anvil' technique,[5] the application of novel melting practices, e.g., plasma flame[6,7] or laser beam[8] heating, and the use of various devices to obtain more extended thin foils, e.g., the 'torsion catapult' technique.[9] One disadvantage of these techniques is that the samples produced are not in a particularly suitable form for quantitative mechanical property measurements. Recently, this particular shortcoming has been eliminated with the introduction of the 'melt spinning',[10] 'melt extraction',[11] 'roller quenching'[12] and centrifugal spin quenching[13] techniques. Melt spinning involves jetting the melt from a small orifice onto the inside surface of a rapidly rotating drum. In melt extraction, the melt source is stationary, and the edge of a rotating disc picks up the melt to form the rapidly quenched filament. Roller quenching is similar to melt spinning except that the jet of molten alloy is directed between a pair of counter-rotating steel rollers. In centrifugal spin quenching, the molten stream is directed against the sloping inner surface of a rapidly rotating drum, such that the liquid flow is controlled by centrifugal and surface tension forces. The continuous thin filaments (round or rectangular in cross section) produced by these techniques experience cooling rates ~10^6°C/sec.

In all of these different melt quenching techniques, melt and substrate are composed of different materials. Another approach in which melt and substrate have identical compositions is the so-called 'self-substrate' technique, where high cooling rates are attained by promoting rapid surface localized melting of a material using an intense energy source. This has been done via electrodischarge machining,[14-16] and more directly by electron beam[17-18] and laser beam heating.[19-22] So far, the use of lasers has been restricted to the pulsed laser systems, in which a high power density is maintained for a very short time. Such a technique is of limited utility for two reasons. First, it is difficult to control surface vaporization and plasma formation. Second, the amount of material that can be processed by this method is small. In what follows, it is shown that these limitations can be overcome by substituting a continuous wave CO_2 gas laser for a pulsed laser. The high rate of surface localized, or 'skin' melting that can be achieved (e.g., 50-650 cm^2/min) by this new technique makes it a practical proposition for commercial exploitation as a method for the surface treatment of metals and alloys.

Experimental

The nature of the interaction of a high power laser beam with a material surface depends primarily on the power density of the incident beam and the interaction time, as will be shown in the following section. As illustrated in Figure 1, the combination of these two factors serves to define operational regimes for various materials processing techniques. At very high power densities of ~10^9 W/cm^2, attainable currently only with pulsed laser equipment, nearly instantaneous surface vaporization occurs on interaction of the beam with the material. If pulse duration is kept to ~10^{-7} sec, typically involving an energy input of the order of 10 J/cm^2, interaction is limited to the surface and the rapid expansion of the vaporized metal produces an effect similar to a blast wave.[23] As a consequence, a shock wave propagates and reflects within the material causing work hardening. The advantage here is that the laser
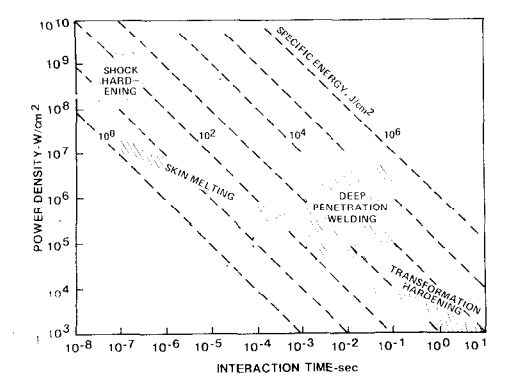
Fig. 1 - Operational regimes for various laser materials processing techniques.
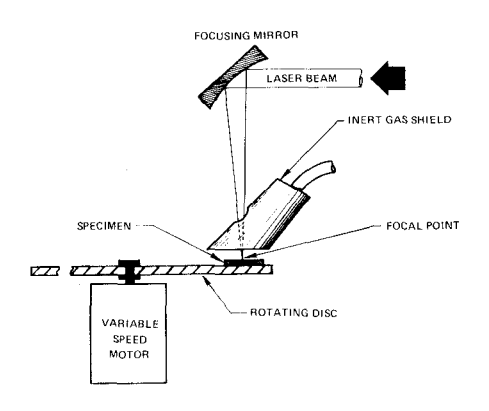

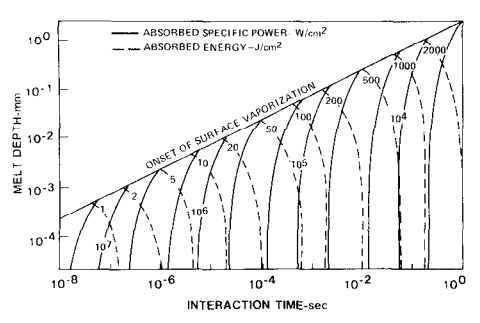Fig. 2 - Schematic of laser skin melting apparatus.

Fig. 3 - Transient surface melting characteristics of nickel.
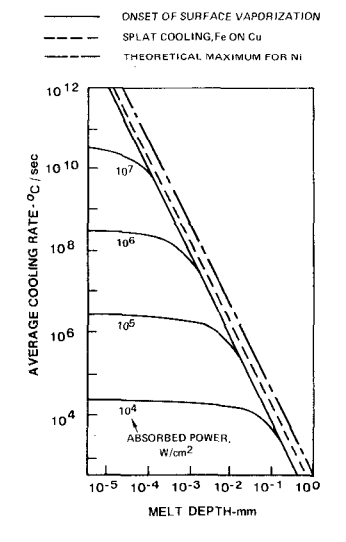

Fig. 4 - Effect of melt depth and power density on average cooling rate.

provides for precise control of the input energy. In the deep penetration welding regime,[24-26] the incident power density must be of ~10^6 W/cm^2 in order to establish the deep penetration mode. Interaction time is relatively longer than for shock hardening since substantial energy must be deposited within the material to induce melting and vaporization to a reasonable depth. In contrast to the low energy input per unit area for shock hardening, therefore, welding requires energy inputs of ~10^4 J/cm^2. For transformation hardening,[27,28] a somewhat lower power density is required in order that some in-depth heating takes place without causing melting to occur at the top surface. The required power density is thus governed by the rate at which thermal energy diffuses through the workpiece material; the value must be high enough to effectively localize the thermal input to a thin region at the surface but low enough to avoid surface melting. Since the thermal interaction must proceed to a specified depth, thermal energy input per unit area required is intermediate between that for shock hardening and deep penetration welding and may typically be of the order of 10^3 J/cm^2. Slightly higher values will induce melting and are therefore suitable for surface alloying.[27] The skin melting region, first explored in the work reported herein, involves high incident

power density of the order of that utilized for welding, but substantially shorter interaction times.[29] With this combination, specific energy inputs may range from 10 to 100 J/cm^2 and the thermal effect is concentrated in a very thin region at the material surface. Localized melting occurs very rapidly in a time period during which little thermal energy penetrates into the base material. This leads to the establishment of extremely sharp temperature gradients which facilitate rapid cooling of the melt following the interaction. Cooling rates approaching 10^6 °C/sec have been estimated to be readily attainable with rates to the range of 10^8 °C/sec possible. As a consequence of the high cooling rate, ultra-microcrystalline or amorphous microstructures may be obtained.

A carbon dioxide laser having a continuous multi-kilowatt output was utilized for the test program. Two sets of cavity optics were employed; the first provided an output beam with a Gaussian energy profile, while the second provided an unstable resonator output with a hollow output beam exhibiting an outer-to-inner diameter ratio (magnification) of two; the former appeared to be the preferred mode. The nominal 7.5 cm diameter beam from the laser was directed toward and focused upon the workpiece by reflective optics, as shown in Figure 2. A 46 cm focal length mirror was used which provided an effective minimum spot diameter of 0.05 cm at the workpiece. At 3 kW, these optics provided a maximum incident power density of approximately 1.5×10^6 W/cm^2, a power density equivalent to that provided by a black body thermal radiative source at 22,800°C. This high power density is essential for localizing the energy input at the material surface, and further promotes effective coupling of the laser energy with the material, despite the initially high reflectivity of metallic surfaces to the 106,000 Å wavelength of carbon dioxide laser radiation. Most tests were conducted at a laser power level of 3 kW. This level is convenient in that it promotes effective beam coupling, but does not create significant plasma generation problems. As noted in Figure 2, plasma suppression was accomplished by means of an inert gas shield, which further prevented atmospheric contamination of the melt. Cooling due to the inert gas flow was estimated to be negligible. A range of skin melt depths was attained by varying the translational speed of the workpiece under the focused beam. Linear speeds from 150 to more than 6000 cm/min were attained by using a variable speed rotating disc with specimens located at a fixed radius on the surface of this disc. This speed range yielded a variation in the incident laser energy per unit length of melt from 1200 down to 30 J/cm. The higher energy inputs were generally utilized in an initial homogenizing pass; specimens were allowed to cool to room temperature prior to a possible second or third skin melt pass. This procedure was used following initial observations from which it was deduced that the material subjected to a high speed pass did not remain in the molten state for a sufficiently long period to promote homogenization of the various phases.

The rotating disc work-handling equipment facilitated irradiation of multiple samples in a single pass. Samples were generally arranged adjacent to each other with their top surfaces located at the focal plane of the beam focusing optics. A smooth machined surface was presented to the focused laser beam. Coatings, such as those employed for some laser surface hardening work, were not used. In general, such coatings are not effective at the high power densities characteristic of the skin melting regime and, further, were avoided since they might lead to contamination of the melt zone. Bulk specimens of ~0.5 cm thick were utilized in order to ensure that essentially no heating of the bulk substrate would occur. This thickness was well above the analytically predicted requirement that the specimen thickness be at least four times the skin melt depth in order to facilitate rapid self-quenching. Most tests were conducted with the specimens initially at room temperature; however, a few tests were made with the specimens initially chilled to liquid nitrogen temperature. Although the results may not have general applicability, it was noted that this prior cooling did not significantly alter the results obtained. This is probably due to the fact that the additional increment in temperature afforded by cooling

from room temperature to liquid nitrogen temperature is not large compared with the temperature difference between that of the liquid at the melting point and the solid at room temperature. Clearly, initial cooling of the specimen becomes more important the lower its melting temperature.

Theory

A heat transfer analysis was performed to determine the effects of process parameters on the rapid melting and cooling process stemming from high power density laser irradiation of metallic materials.[30] A one-dimensional, finite element technique was employed for the transient cooling process, and results of an analog computation[31] were used for the surface melting (heating) phase. The method of analysis involved selection of laser power density and interaction time and, using the results given in Ref. 30, determination of the resultant melt depth and temperature profiles in the molten and solid regions. These temperature profiles were used as initial conditions in the finite element program which was used to compute the transient cooling of the material for the selected power and interaction time. Finally, an average cooling rate was calculated for the period from the cessation of power input to the time at which the material surface cooled to 816°C.

Figure 3 illustrates the transient surface melting characteristics for nickel. The solid lines indicate melt depth versus interaction time for various power densities. Interaction time is defined as the time required for the incident laser beam to traverse one spot diameter, and is computed as the ratio of spot diameter to beam sweep speed, D/V. The period is initiated from a uniform initial temperature of 21°C and thus includes the time during which the material is heated up to and through the melting point. Subsequent to the onset of melting, the advance of the melt interface was found to be approximately linear with time. The dashed lines in Figure 3 indicate constant specific energy inputs to the material and are computed as the product of the absorbed specific power and the interaction time. It can be seen that the specific energy required to obtain a given melt depth decreases as power density is increased and interaction time is decreased. The reason for this, of course, is that at higher power densities less time is available for heat conduction into the solid, i.e., the energy is more concentrated in the melt. Thus, increased melting efficiency is not the only benefit of higher power densities; the steeper temperature gradients in the material also enhance more rapid cooling.

Figure 4 shows the effect of melt depth on average cooling rate for selected values of power density. It can be seen that there is a maximum cooling rate for a given absorbed power density corresponding to the limiting case in which melt depth approaches zero. This maximum cooling rate was shown analytically to increase with the square of the power density. For a constant melt depth, the increase in cooling rate with absorbed specific power is a consequence of the increased steepness of the temperature gradients. Roughly, doubling the power density doubles the cooling rate for a given melt depth. Figure 4 also shows that a minimum cooling rate exists at the point corresponding to the onset of surface vaporization (maximum melt depth for a given power density). For reference, Figure 4 also shows the theoretical maximum cooling rate in nickel as a function of melt depth as well as results for the splat cooling of iron on a copper substrate.[32] The former curve is obtained by considering that all of the absorbed energy is initially concentrated in the melt, such that a temperature discontinuity equivalent to the melt temperature exists at the solid-liquid interface. It is noteworthy that the theoretical maximum cooling rate, the splat cooling rate, and the average cooling rate at the onset of surface vaporization all follow an inverse square law with melt depth. The effects of convection and radiation heat losses on cooling rate were examined for a wide range of parameters. Even at a radiative emissivity of 1.0 and a high convective heat transfer film coefficient of 0.57 W/cm^2 °C, the average cooling rate was not changed by any more than a few percent for absorbed power densities of 10^5 W/cm^2 and greater. The obvious conclusion is that when high power

densities are utilized for skin melting, the subsequent rapid cooling phenomenon is controlled by conduction heat transfer.

A brief cooling rate analysis was conducted for aluminum to provide an indication of the influence of material thermal diffusivity on cooling rate. It was shown that while the theoretical maximum cooling rate in aluminum, based on cooling to one-half of the melt temperature, was 70% higher than for nickel, the maximum cooling rate as melt thickness approaches zero was somewhat lower for the same absorbed specific power. The reason for this is that if all the energy could be concentrated in the melt, the more highly conducting aluminum would cool faster. However, due to the higher conductivity, surface heating energy is distributed over a larger initial volume in aluminum such that reduced temperature gradients and consequent reduced cooling rates are obtained. It should be noted, however, that the general dependence of cooling rate on thermal diffusivity cannot be inferred from this single comparison, since the rate is influenced by a variety of factors including initial and final temperatures.

Discussion of Results

Splat quenching techniques typically yield very high cooling rates $> 10^5$ °C /sec. Controlled quenching at lower rates is difficult to achieve by such techniques, and is normally not attempted. Laser skin melting, on the other hand, provides a convenient method for obtaining a wide range of cooling rates (10^3- 10^8 °C/sec) in a perfectly controllable manner. It is this feature that makes the skin melting technique such a powerful tool for determining the dependence of the microstructure on cooling rate in a given alloy system. In what follows it will be shown that some novel microstructures can be developed under the moderate cooling rates easily attainable by skin melting, but not readily accessible to conventional splat quenching techniques. Selected alloys for the splat quenching and skin melting experiments included representative compositions from three broad classes of nickel-base alloys; namely, the low melting point TLP-type eutectic alloys, the γ' particle strengthened superalloys, and the new generation of filamentary, or lamellar eutectic superalloys.

Splat Quenching

Both single and twin substrate techniques were used to obtain samples of rapidly quenched alloys. The response of these different alloys to splat quenching will be summarized.

The low melting point brazing alloys typically gave an amorphous, or microcrystalline structure, depending on cooling rate. Figure 5 shows such structures in splat quenched TLP-21; nominal composition Ni-15Co-15Cr-5Mo-2.75B. In the amorphous condition, the microstructure is featureless except for the presence of a few rosette-shaped crystalline particles, Figure 5a; the corresponding electron diffraction pattern shows diffuse rings with the strong inner ring centered on the position of the 111 ring of the crystalline material, Figure 5b. In the partially decomposed or microcrystalline condition, the microstructure is spherulitic dendritic, Figure 5c, with dendrites composed of nickel solid solution (γ phase) and interdendritic interstices containing fine particles of $M_{23}B_6$, Figure 5d. This latter phase is not found in the normal as-cast structure, which consists of γ + Ni_3B eutectic, plus traces of other complex boride phases. The effect of ageing on the decomposition of the amorphous alloy has been examined in detail and will be reported elsewhere.

In sharp contrast to the behavior of the low melting point B-rich eutectic alloys, an amorphous structure was not obtained by splat quenching of the γ' particle strengthened nickel-base superalloys. Instead, these alloys invariably gave a fine dendritic structure, with varying degrees of microcrystallinity and phase decomposition. In all cases, no evidence was found for γ' precipitation, but a strong indication was obtained for the presence of short-
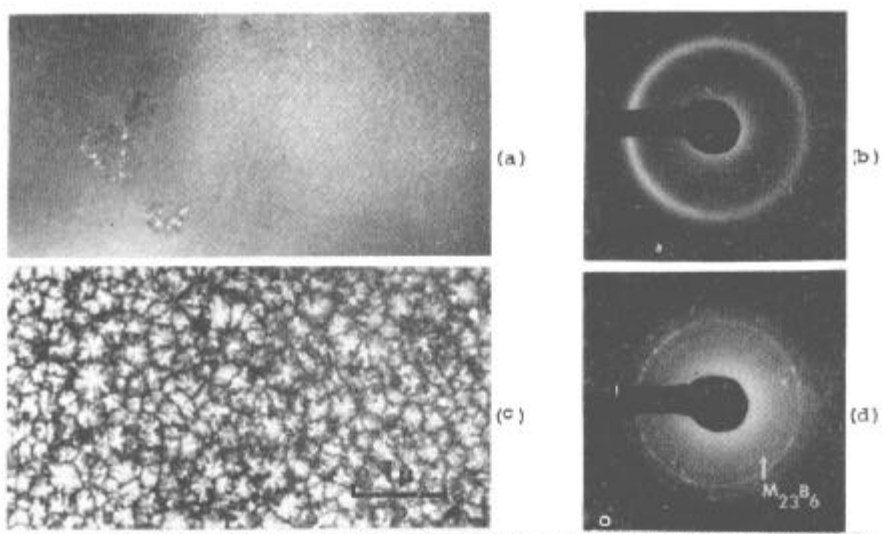
Fig. 5 - Transmission electron micrographs and corresponding electron diffraction patterns of splat quenched TLP-21; (a) and (b) amorphous material, (c) and (d) microcrystalline material.
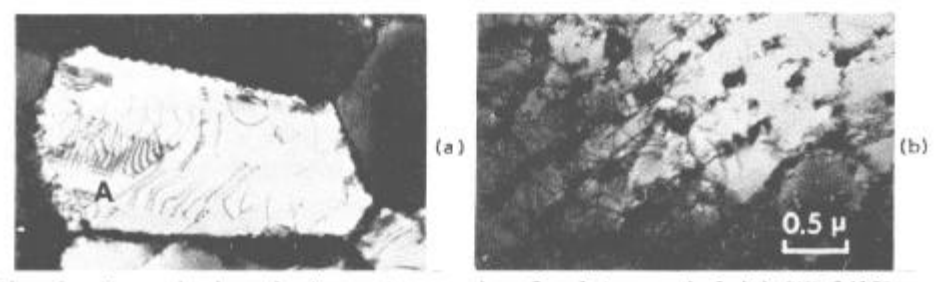

Fig. 6 - Transmission electron micrographs of splat quenched (a) PWA-1418L, (b) B-1900.
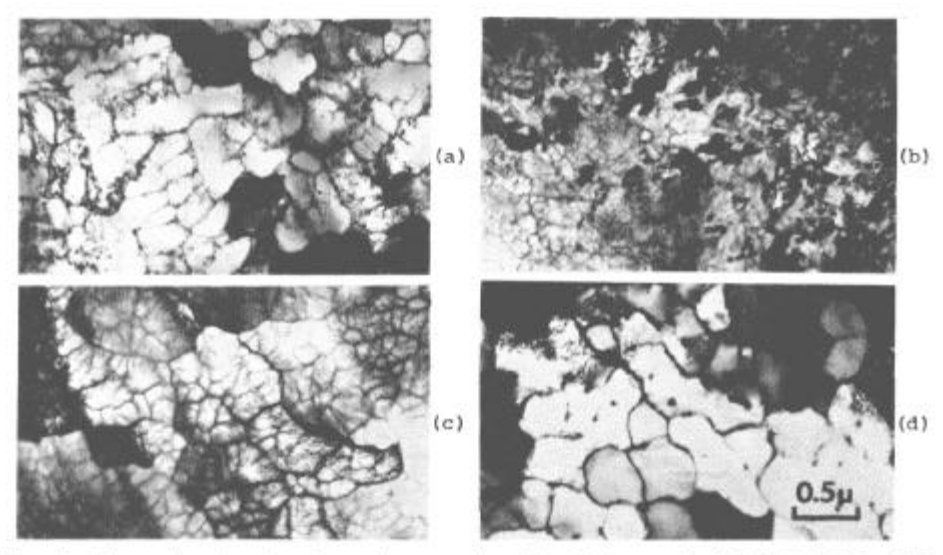

Fig. 7 - Transmission electron micrographs of splat quenched (a) CoTaC-3, (b) CoTaC-33, (c) NiTaC-13 and (d) $\gamma/\gamma'-\delta$

range order in the γ phase. Evidence for this in PWA 1418L (low carbon modification of Mar-M200) is shown in Figure 6a, where many of the dislocations are arranged as loosely coupled pairs. In particular, note the increase in pair spacing for successive pairs in the sequence indicated at A. This is in accord with theoretical predictions for dislocation motion in an alloy containing short-range order.[33] Such a microstructure is probably typical of alloys where the carbon content does not exceed the solid solubility limit in the alloy. In other alloys, where the carbon content is higher and sufficient, say, to yield ~2 vol. pct. of MC carbide in the normal as-cast microstructure, complete suppression of the precipitation of carbide phase during splat quenching is not always achieved. The presence of fine particles of the carbide phase modifies the dislocation structure developed within the grains during quenching. This is shown for splat quenched B-1900 in Figure 6b. Apparently, in this case, the dislocations generated by the quenching stresses became trapped by interaction with the carbide particles, thereby forming a pronounced dislocation substructure within each grain. Such is not the case in PWA 1418L, where dislocations evidently glide freely across the grains, with the grain boundaries acting both as sources and sinks for dislocations.

Splat quenching of the eutectic superalloys gave a variety of microstructures, depending not only on cooling rate, but also on alloy composition. Figures 7a and 7b compare the microstructures of two different compositions in the CoTaC series of alloys. As shown, the effect of replacing some of the Ta with W is to refine the grain structure and the distribution of MC carbide particles. In the very fine grained region in Figure 7b, precipitation of carbides has been completely suppressed, despite the fact that the equilibrium volume fraction in the alloy is ~13 pct. In a representative alloy in the NiTaC series, precipitation of carbides occurs uniformly throughout the structure on an extremely fine scale, Figure 7c. The fact that in this alloy each matrix reflection was associated with a diffuse MC carbide reflection can be taken as evidence for 'coherent' precipitation of MC carbide in the γ matrix. In the γ/γ'-δ eutectic alloy, precipitation of the γ' phase was suppressed but not that of the δ-phase, Figure 7d. As was the case for the carbides, the presence of the δ-phase served to stabilize the dislocation substructure within the relatively large grain structure of the splat-quenched material.

Skin Melting

In skin melting, the crystalline substrate necessarily is in intimate contact with the melt. This raises the question as to whether the presence of favorable nucleation sites for crystallization would prevent the undercooling necessary to achieve an amorphous structure. Test experiments on a low melting point eutectic alloy (Pd-4.2Cu-5.1Si) demonstrated that, under appropriate conditions of fast cooling, this alloy can be made amorphous by skin melting. In this instance, the skin melted layer (~0.18 mm maximum in thickness) was obtained with an incident power density of 6×10^6 W/cm^2 and an interaction time of 3×10^{-5} sec. As shown in Fig. 8, within the skin melted region, there are no discernible microstructural features, in contrast to the eutectic structure in the substrate. One manifestation of the non-crystalline amorphous nature of the material is the symmetrical pattern of curved shear bands formed around hardness indentations, Figure 8d. Another manifestation is the vein-like character of the fracture surface, Figure 8c. Confirmatory evidence was obtained by TEM; the thin foils had a speckled appearance and the electron diffraction pattern showed diffuse rings, Figure 8b.

Similar tests carried out on low melting point TLP-type eutectic alloys gave no clear indication of an amorphous transition by skin melting, even in thin sections (~0.025 mm) that had cooled at high rates. More typically, the result of skin melting of these alloys was the formation of either an ultrafine dendritic structure, with varying degrees of phase decomposition, or an extremely fine eutectic structure. Examples of these two types of behavior were found in the three boron-rich nickel-base alloys shown in
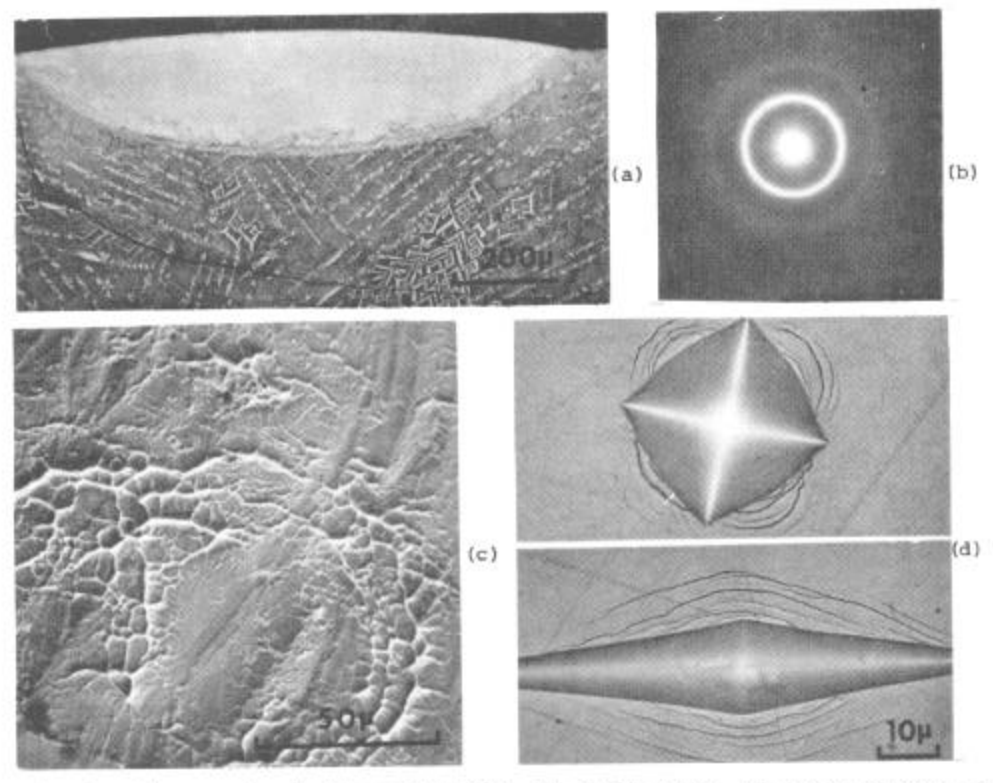
Fig. 8 - Micrographs of skin melted Pd-4.2Cu-5.1Si alloy; (a) cross section of skin melt, (b) electron diffraction pattern, (c) fracture surface, and (d) hardness indentations.
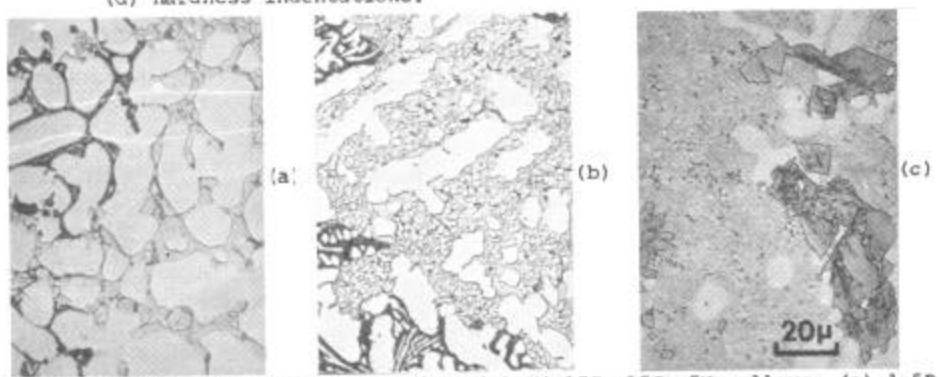

Fig. 9 - Micrographs of a series of B-rich Ni-15Co-15Cr-5Mo alloys; (a) 1.5B, (b) 2.75B and (c) 4.0B.
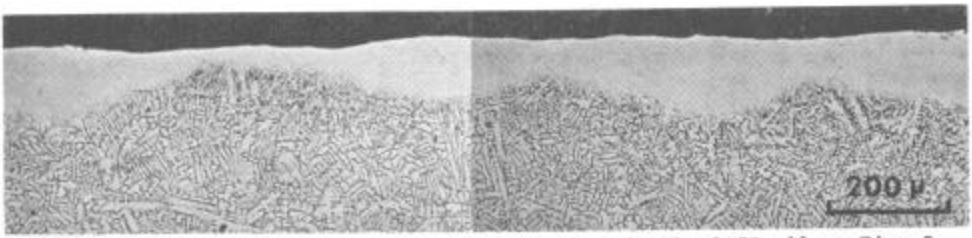

Fig. 10 - Overlapping skin melts at 3kW-25 cm/sec in the 1.5B alloy, Fig. 9. VHN of skin melt = 600 kg/mm^2.

Figure 9. Alloy (b) has the preferred composition for TLP-21, an interlayer composition used for diffusion bonding of Udimet 700. Alloys (a) and (c) are, respectively, low and high boron modifications of this multicomponent alloy. As indicated in Figure 9, increasing the boron in this series of alloys increases the volume fraction of γ + Ni$_3$B eutectic, at the expense of primary γ. Alloy (c) contains a mixture of two primary phases (γ + M$_3$B$_2$), whereas alloys (a) and (b) contain only one primary phase (γ). All three alloys responded to skin melting by forming featureless regions, at least under the optical microscope. Figure 10 shows a series of overlapping passes in alloy (a), whereas Figure 11 shows a series of parallel passes with varying interaction time in alloy (c). The most sharply distinguishing feature of these two examples is the extensive cracking in alloy (c), and the absence of cracking in (a). This has nothing to do with variations in skin melting parameters, but merely reflects the different strengths and ductilities of the substrates and skin melted regions. Both the substrate and skin melted regions are very hard in alloy (c), whereas they are much softer in alloy (a). Thus, cracking is avoided, or at least reduced, in (a) because of the ability of the material to undergo plastic deformation in response to the thermal strains developed during quenching. In (c), cracking typically took the form of a single longitudinal mid-rib crack, with many short transverse cracks, Fig. 11d. Alloy (b) also showed extensive cracking, which is consistent with the presence in this alloy of a large volume fraction of the hard, brittle γ + Ni$_3$B eutectic, comparable with that in alloy (c). Although the microstructures of the skin melted regions in these alloys appeared to have no structure, close examination by SEM and TEM techniques showed that this was not the case. On the contrary, alloys (a) and (b) were composed of an ultra-fine dendritic structure, Fig. 12a, whereas alloy (c) possessed a remarkable ultra-fine filamentary eutectic structure, Figure 12b. A general refinement in these structures was noted with decreasing thickness of the melt zone, as would be expected in view of the higher cooling rates. Under polarized light, with the material in the as-polished condition, a columnar grain structure became visible in alloy (c), Figure 13. Using this technique, it was shown that the superposition of two or more skin melting passes resulted in epitaxial growth, albeit with a thin transition layer of what appeared to be a spheroidized structure. A similar transition microstructure also occurs quite naturally at the interfaces between the melt zone and its substrate. In alloys (a) and (b), the transition zone was quite wide, reflecting the wide melting range of TLP-21 (1060°C solidus-1200°C liquidus). Selective melting of the eutectic, leaving the dendrites unmelted, can be seen in the transition zone of alloy (a) in Figure 10.

Skin melting experiments performed on the eutectic superalloys gave a broad spectrum of microstructures, which differed mainly in degree, or scale, rather than in kind. Under high cooling rates, the microstructure typically was composed of a fairly uniform distribution of MC carbide particles embedded in a solid solution matrix phase, similar to that found in splat quenched material. Under more moderate cooling rates, the structure was distinctly dendritic, with the MC carbide phase concentrated exclusively in the interdendritic interstices. These two representative types of microstructures are shown for a CoTaC-type eutectic alloy in Figure 14. In the skin melted pass at 3kW - 51 cm/sec, Figure 14a, the MC carbide phase occurs as discrete particles having a platelet morphology, whereas in the skin melted pass at the lower cooling rate (3kW - 12.7 cm/sec) Figure 14b, the carbide phase has a filamentary morphology. The very fine scale of the filamentary eutectic structure can be appreciated by reference to Figure 14c, which shows the transition zone between the skin melted layer and its substrate; the latter was solidified under carefully controlled plane front conditions. This abrupt change in microstructure is illustrative of the sensitivity of the microstructure in this alloy to solidification conditions. It is well known that a high ratio of temperature gradient to solidification rate, (G/R), is a prerequisite for coupled growth in this multicomponent, mono-variant eutectic alloy. Further tests are being conducted to determine if it is at all possible to generate a fully eutectic structure on the scale shown in Figure 14b. Another noteworthy feature with respect to the
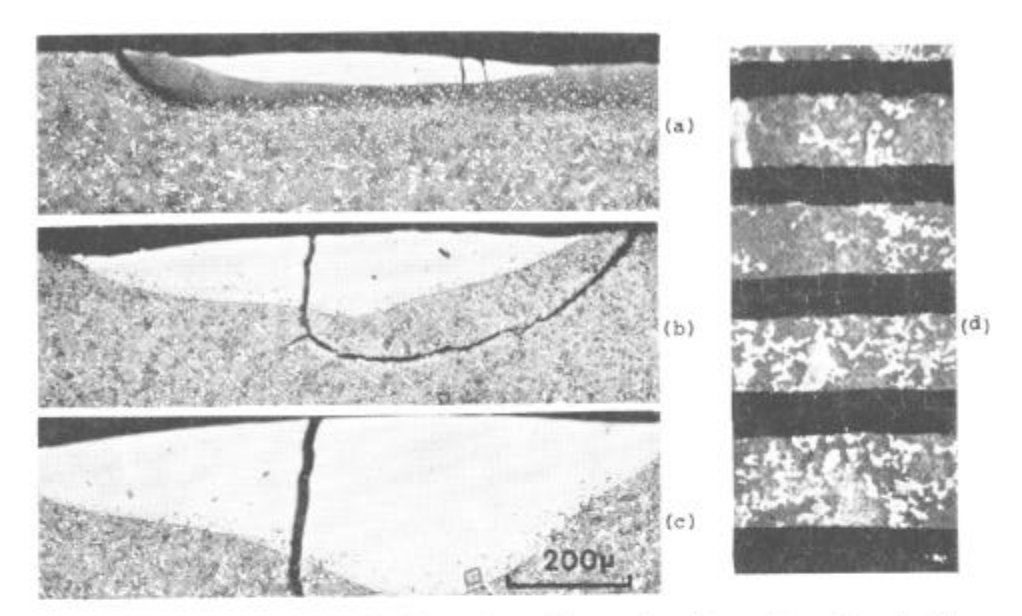
Fig. 11 - Series of parallel skin melts with varying interaction time in the 4.0B alloy, Fig. 9; (a) 3kW-50 cm/sec, (b) 3kW-25 cm/sec, (c) 3kW-10 cm/sec and (d) top view of skin melts showing surface cracking. VHN of skin melts = 1300 kg/mm^2.
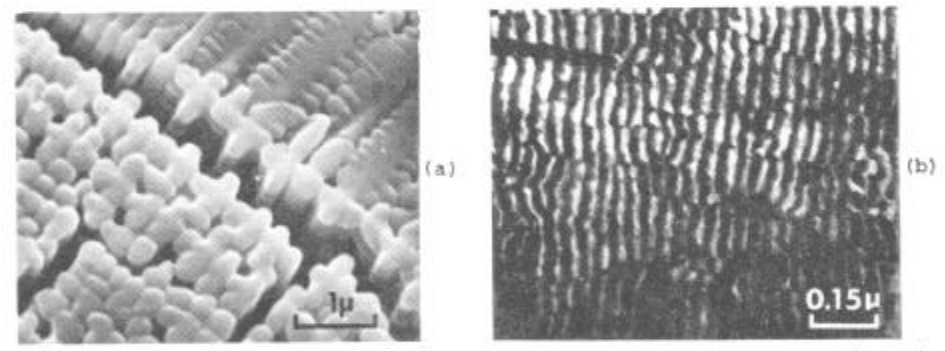

Fig. 12 - Micrographs of skin melted (3kW-12.5 cm/sec) B-rich alloys shown in Fig. 9; (a) scanning electron micrograph of 1.5B alloy, (b) transmission electron micrograph of 4.0B alloy.

Fig. 13 - Optical micrograph under polarized light of 4.0B alloy, Fig. 9, showing columnar grain structure in the skin melted region.
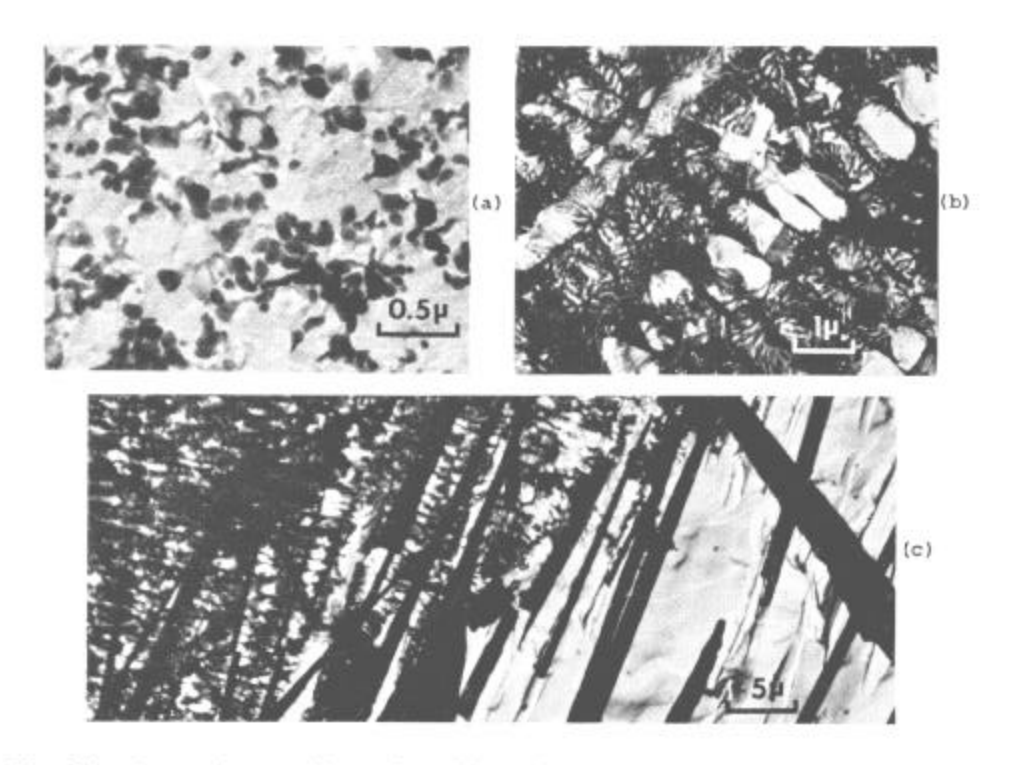
445

Fig. 14 - Extraction replicas of a skin melted CoTaC-3 alloy; (a) 3kW-51 cm/sec,
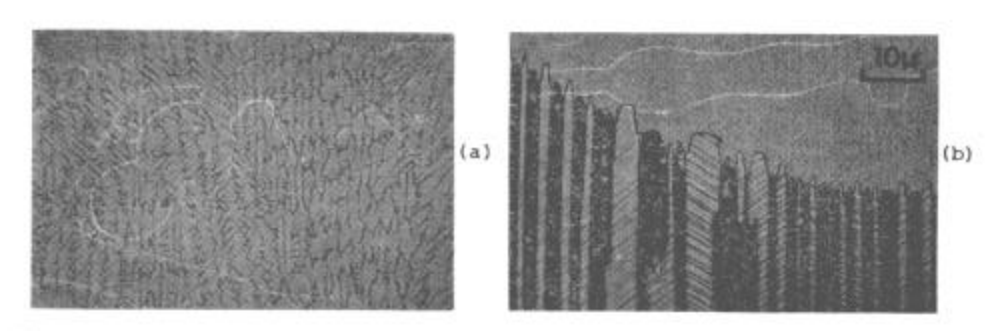(b) and (c) 3 kW-12.7 cm/sec.

Fig. 15 - Micrographs of skin melted γ/γ'-δ; (a) skin melted region, (b) inter-
face between skin melted region and substrate showing twinning in
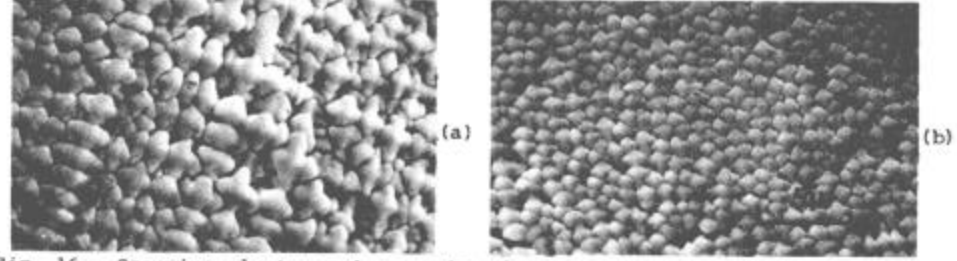substrate δ-phase.

Fig. 16 - Scanning electron micrographs of external surface of skin melted PWA-
1418L; (a) 3kW-30 cm/sec, (b) 3kW-96 cm/sec.

response of these alloys to skin melting was the absence of cracking, both in the skin melts and in the substrate heat affected zones. Apparently, in these alloys, the solid solution matrix phase is sufficiently ductile as to ensure the necessary plastic accommodation in both skin melt and substrate during cooling from the melt.

In contrast to the behavior of the carbide eutectic alloys, skin melting of the $\gamma/\gamma'-\delta$ eutectic did not give a well organized, fine-scale lamellar eutectic structure. In this case, the typical result was the development of a fine dendritic structure, Figure 15a, with some precipitation of γ' and δ, but particularly the δ phase. Moreover, cracking was observed in the skin melted regions, especially in the deeper skin melts, but not in the substrate. Evidently in this case, plastic deformation occurs quite freely in the substrate during fast cooling, and evidence for this is shown in Figure 15b. On the other hand, deformation is inhibited in the skin melted regions because of precipitation of γ' and δ, which sharply increases the strength of the material.

Skin melted γ' precipitation hardened superalloys invariably exhibited dendritic growth. Direct evidence was obtained by SEM observations on the external surface along the center line of the skin melt, where, due to inadequate melt feeding, the dendritic structure stood out in sharp relief. Observations made in this way showed that the scale of the dendritic structure decreased with increasing cooling rate, or decreasing skin melt depth, as would be expected, Figure 16. Comparable structures were observed in transverse metallographic sections; moreover, strong indications were found for regrowth of certain, if not all, of the partially-consumed substrate grains residing at the original melt/substrate interface. In monocrystalline material, such oriented overgrowth, or epitaxial growth, appeared to be particularly favored on a cube oriented substrate, apparently because the normal to the substrate coincides with a fast-growing dendrite direction; namely <001>. This is shown for PWA 1418L in Figure 17. The rather dramatic refinement in the scale of the dendritic structure following the first skin melting pass at 4 kW – 3.5 cm/sec is quite obvious in this micrograph. A further refinement in structure occurs in the two additional overlapping skin melting passes just visible at the top of the micrograph. When misoriented grains are present in the epitaxial zone, Figure 17 indicates that these tend to be eliminated by faster growth of the more favorably oriented cube-oriented grains. Misoriented grains are frequently nucleated in the vicinity of γ/γ' eutectic located at the melt/substrate interface. Examination of the various interfaces in the skin melted material, Figure 17b, shows that in the first pass the structure develops by cellular growth, and as the gradient falls off this degenerates into cellular dendritic and finally dendritic growth. In the second and third passes, the cellular mode of solidification is predominant. More compelling evidence for epitaxial growth was obtained from observations on the external surface of the skin melted material. As shown in Figure 18, the surface is covered with a network of intersecting slip bands, which are continuous despite extraordinary variations in the general appearance of the dendritic structure, Figures 18b and 18c. Slip bands in the same orientations were also visible in the adjacent substrate. Clearly, this would not be possible unless the entire skin melted material had the same orientation as the monocrystalline substrate. Obviously, this deformation represents the plastic accommodation that must occur during skin melting if cracking is to be avoided. No cracking, in fact, was found in the skin melted PWA 1418L. Oriented overgrowth without cracking has also been seen in other orientations in this material; notably in [110] and [112] substrate orientations.

Applications

It is not difficult to envisage many possible applications for laser skin melting. In principle, almost any component, or monolithic structure, whose performance or properties are surface limited can benefit from skin melting. For example, a turbine blade may possess excellent creep properties in the air-
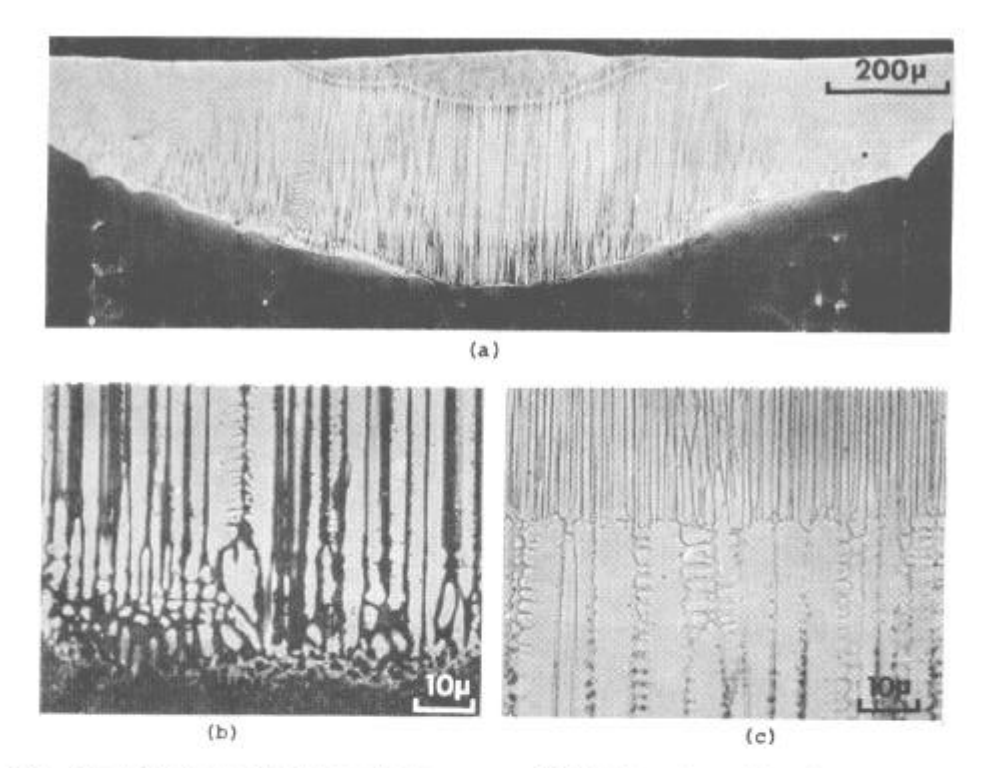
Fig. 17 - Superimposed skin melting passes (3kW-3.5 cm/sec, 60 cm/sec and 81 cm/sec) in a [100] oriented PWA 1418L monocrystal, showing evidence for epitaxial growth; (a) general view, (b) substrate/skin melt interface, (c) interface between successive passes.
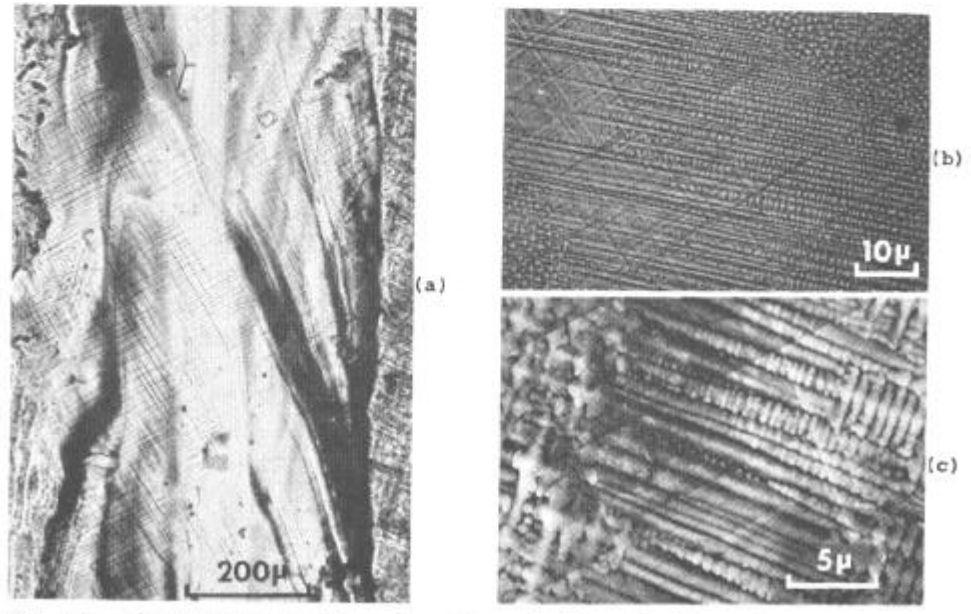

Fig. 18 - Micrographs of external surface of skin melted PWA 1418L in the cube orientation showing evidence for two sets of intersecting slip bands; (a) and (b) light micrographs, (c) scanning electron micrograph.

foil section, and yet the low-cycle fatigue properties of the root section may be inadequate, say, as a result of an unfavorable distribution of MC carbides at the free surface. Surface treatment by laser skin melting may be employed to uniformly disperse the carbides on a much finer scale, which might possibly improve the fatigue properties by making it more difficult to initiate cracks. Again, in the same application, the blade tip may be subject to excessive erosion. This problem could conceivably be resolved by melting in an overlay coating that possesses the desired properties. Overlay coatings might also benefit by skin melting to further protect the airfoil from oxidation and/or corrosion. These few examples are illustrative of the potential of the skin melting technique for the surface treatment of superalloys. Similar advantages may be gained in other areas of structural applications, such as in the surface treatment of tools and bearings.

Finally, it should be mentioned that processing by skin melting is not limited to materials for structural applications. Interesting possibilities exist for the surface treatment of semi-conductors to promote epitaxial growth, and for the processing of materials for magnetic and superconducting applications.

References

1. P. Duwez, R. H. Willens and W. Klement, J. Appl. Physics, 31, (1960), 1136.

2. P. Duwez and R. H. Willens, Trans. Met. Soc. AIME, 227, (1963), 362.

3. R. H. Willens and E. Buehler, Trans. Met. Soc. AIME, 236, (1966), 171.

4. P. Pietrokowsky, Rev. Sci. Inst., 34, (1963), 445.

5. P. Ramachandrarao, D. Banerjee and T. R. Anantharaman, Met. Trans., 1, (1970), 2655.

6. M. Moss, D. L. Smith and R. A. Lefever, Appl. Phys. Letters, 5, (1964), 120.

7. K. Yamauchi and Y. Nakagawa, Jap. J. Appl. Phys., 10, (1971), 1730.

8. R. Krepski, K. Swyler, H. R. Carleton and H. Herman, J. Matls. Sci., 10, (1975), 1452.

9. R. Roberge and H. Herman, Mat. Sci. and Eng., 3, (1968), 62.

10. R. Pond and R. Maddin, Trans. Met. Soc. AIME, 245, (1969), 2475.

11. R. E. Maringer and C. E. Mobley, J. Vac. Sci. Technology, 11, (1974), 1067.

12. H. S. Chen and C. E. Miller, Rev. Sci. Inst., 41, (1970), 1237.

13. H. S. Chen and C. E. Miller, Mat. Res. Bull., 11, (1976), 49.

14. K. Mutsuzaki, M. Suzuki and E. Kawai, J. Japan Inst. Light Metals, 27, (1963), 424.

15. H. Kaneko and J. Ikeuchi, 1st Int. Conf. Electrodischarge Machining (Tokyo, Japan EDM Society), (1965), 23.

16. H. Ruppersberg and H. Bold, Metall., 26, (1972), 34.

17. W. Hiller, La Metallurgie, 100, (1968), 35.

18. B. Lux and W. Hiller, Prakt. Met., 8, (1971), 218.

19. H. Jones, Mat. Sci. Eng., 5, (1969), 1.

20. L. I. Mirkin, Izvest. Vuz Chern. Met. #2, (1971), 98.

21. M. Laridjani, P. Ramachandrarao and R. W. Cahn, J. Matls. Sci., 7, (1972), 627.

22. W. A. Elliott, F. P. Gagliano and G. Krauss, Appl. Phys. Letters, 21, (1972), 23.

23. A.H. Clauer and B. P. Fairand, J. of Metals, 27, #12, (1975), A51.

24. C. O. Brown and C. M. Banas, 52nd Annual Meeting, AWS, San Francisco, April 26-29, 1971.

25. E. V. Locke, E. D. Hoag And R. A. Hella, IEEE Journal of Quantum Electronics, 8, #2, (1972).

26. E. M. Breinan, C. M. Banas and M. A. Greenfield, IIW Document #IV-181-75, June 1975.

27. R. A. Hella and D. S. Gnanamuthu, Annual Meeting AWS, St. Louis, May 10-14, 1976.

28. E. M. Breinan, L. E. Greenwald, C. M. Banas, J. W. Davies and J. P. Carstens, Proc. ASM Conf. on Laser Surface Treatment for Automotive Applications, Detroit, Feb. 17, 1976.

29. E. M. Breinan, B. H. Kear, C. M. Banas and L. E. Greenwald, Proc. ASM Conf. on Laser Treatment for Automotive Applications, Detroit, Feb. 17, 1976.

30. L. E. Greenwald, United Technologies Research Center Report R75-111321-1, October 1975.

31. M. I. Cohen, Journal of the Franklin Institute, 283, #4, (1967), 271.

32. R. C. Ruhl, Mat. Sci. Eng., 1, (1967), 313.

33. J. B. Cohen and M. E. Fine, J. Phys. Radium, 23, (1962), 749.